View metadata, citation and similar papers at core.ac.uk

brought to you by CORE

provided by UCL Discovery

Biochemical Journal (2016) **473** 4473–4491
DOI: 10.1042/BCJ20160744

PORTLAND PRESS

Research Article

Domain structure of human complement C4b extends with increasing NaCl concentration: implications for its regulatory mechanism

Ka Wai Fung[1], David W. Wright[1], Jayesh Gor[1], Marcus J. Swann[2] and Stephen J. Perkins[1]

[1]Department of Structural and Molecular Biology, University College London, Darwin Building, Gower Street, London WC1E 6BT, U.K. and [2]Swann Scientific Consulting Ltd, 110 Sandy Lane, Lymm WA13 9HR, U.K.

Correspondence: Stephen J. Perkins (s.perkins@ucl.ac.uk)

OPEN ACCESS

During the activation of complement C4 to C4b, the exposure of its thioester domain (TED) is crucial for the attachment of C4b to activator surfaces. In the C4b crystal structure, TED forms an Arg^{104}–Glu^{1032} salt bridge to tether its neighbouring macroglobulin (MG1) domain. Here, we examined the C4b domain structure to test whether this salt bridge affects its conformation. Dual polarisation interferometry of C4b immobilised at a sensor surface showed that the maximum thickness of C4b increased by 0.46 nm with an increase in NaCl concentration from 50 to 175 mM NaCl. Analytical ultracentrifugation showed that the sedimentation coefficient $s_{20,w}$ of monomeric C4b of 8.41 S in 50 mM NaCl buffer decreased to 7.98 S in 137 mM NaCl buffer, indicating that C4b became more extended. Small angle X-ray scattering reported similar R_G values of 4.89–4.90 nm for C4b in 137–250 mM NaCl. Atomistic scattering modelling of the C4b conformation showed that TED and the MG1 domain were separated by 4.7 nm in 137–250 mM NaCl and this is greater than that of 4.0 nm in the C4b crystal structure. Our data reveal that in low NaCl concentrations, both at surfaces and in solution, C4b forms compact TED–MG1 structures. In solution, physiologically relevant NaCl concentrations lead to the separation of the TED and MG1 domain, making C4b less capable of binding to its complement regulators. These conformational changes are similar to those seen previously for complement C3b, confirming the importance of this salt bridge for regulating both C4b and C3b.

Introduction

In the complement system of innate immunity, its activation through the classical and lectin pathways through C4b is distinct from its activation in the alternative pathway through C3b. The classical pathway requires binding of C1q to antibody–antigen complexes on pathogen surfaces, whereupon the serine protease $C1r_2C1s_2$ is activated [1]. The lectin pathway involves the interaction of mannose-binding lectin to mannose residues on pathogen surfaces, whereupon mannose-binding lectin-associated serine protease (MASP)-1 and MASP-2 are activated [1]. These activated proteases cleave complement C4 (205 kDa) into C4a (9 kDa) and C4b (188 kDa). Recent crystal structures for C4 and C4b provided high-resolution information on their structures and functions [2,3]. C4 and C4b possess 13 and 12 domains, respectively, including a core of eight macroglobulin domains (MG1–MG8). The cleavage of the C4a fragment (the anaphylatoxin domain) from C4 results in a large conformational change in its domain structure, in which the thioester domain (TED) moves away from its buried position in C4 next to the MG8 domain to make contact with the MG1 domain (Figure 1A). By this, a salt-bridge interaction between Arg^{104}–Glu^{1032} is formed, and the reactive thioester bond within the TED is exposed for nucleophilic attack on its targets. Activated C4b is thus capable of attaching covalently to hydroxyl or amine groups on pathogenic surfaces, thus acting as an opsonin.

Received: 9 August 2016
Revised: 11 October 2016
Accepted: 13 October 2016

Accepted Manuscript online: 13 October 2016
Version of Record published: 25 November 2016

© 2016 The Author(s). This is an open access article published by Portland Press Limited on behalf of the Biochemical Society and distributed under the Creative Commons Attribution License 4.0 (CC BY).

Biochemical Journal (2016) 473 4473–4491
DOI: 10.1042/BCJ20160744

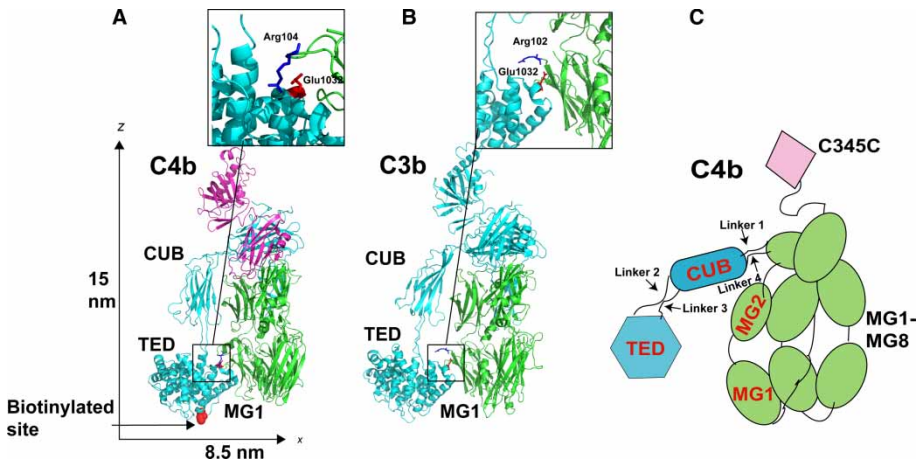

Figure 1. Crystal structures of human C4b and C3b.

(**A**) The α, β and γ chains of C4b in its crystal structure (PDB ID: 4XAM) are shown in green, cyan and pink, respectively. The biotinylation site at Cys991 in the thioester bond of TED is shown as red spheres. The length and width of C4b are indicated on its *z*-axis and *x*-axis as shown. Inset: The Arg^{104}–Glu^{1032} salt bridge between TED (cyan) and the MG1 domain (green). (**B**) The α and β chains of C3b in its crystal structure (PDB ID: 2I07) are shown as green and cyan, respectively. Inset: the Arg^{102}–Glu^{1032} salt bridge between TED (cyan) and the MG1 domain (green). (**C**) Schematic cartoon of the 12 domains in C4b. The MG1–MG8, C345C and TED/CUB domains are in green, purple and blue, respectively. For the scattering fits, linkers 1 and 4 connect the CUB–MG8 domains, and linkers 2 and 3 connect the TED–CUB domains.

Complement C4 is structurally homologous to complement C3 in the alternative pathway and to complement C5, all three of which belong to the α_2 macroglobulin (α_2M) superfamily with similar domain structures [4]. The same large conformational change in TED occurs between inactive complement C3 and its activated form C3b [5,6]. In C3, TED is partly buried in contact with the MG8 domain. In C3b, TED and the MG1 domain make contact with each other through an Arg^{102}(MG1)–Glu^{1032}(TED) salt bridge (Figure 1B). In contrast, even though inactive C5 showed the same buried TED–MG8 arrangement seen in C3 and C4 [7], the crystal structure of C5b in its complex with C6 showed that its TED and MG1 domains were separated by up to 5 nm and were not in contact (Figure 1C) [8]. Protein crystal growth requires non-physiological conditions such as low or high salt concentrations, and these may induce non-native protein conformations within the crystal lattice. The first evidence of different conformations for TED in C3b came from solution structural analyses of C3u, the thioester-hydrolysed form of C3, which has C3b-like functional properties [9]. Different conformations in C3u were revealed by analytical ultracentrifugation (AUC) and small angle X-ray scattering (SAXS) performed in low salt (50 mM NaCl) and physiological salt (137 mM NaCl). These corresponded to a compact TED–MG1 conformation in low salt and an extended TED–MG1 arrangement in physiological salt. Solution structures for C3b in low and physiological salt also showed the same outcome by AUC and SAXS [10]. For C3b, mutagenesis established that the compact structure was stabilised by the Arg^{102}(MG1)–Glu^{1032}(TED) salt bridge. In the C3S wild-type allotype of C3b, this bridge was formed in low salt, but became dissociated in physiological salt (Figure 1B) [10]. This weakly formed salt bridge is important for C3b regulation by its cofactor Factor H, because this salt bridge stabilised the interaction with Factor H. In the C3F disease-risk allotype, when Arg^{102} is replaced by Gly^{102}, this salt bridge is no longer possible and C3b is now resistant to Factor H-mediated degradation. C3F is associated with blindness through age-related macular degeneration (AMD) and renal failure through atypical haemolytic uraemic syndrome (aHUS) [11].

In C4b, the corresponding salt-bridge residues were seen to be Arg^{104}(MG1) and Glu^{1032}(TED) (Figure 1A). Because of the importance of this salt bridge for C3b and C4b regulation in the three pathways for complement activation, we set out to determine whether C4b presented a compact solution conformation in low salt and an extended one in physiological salt. In low NaCl concentration conditions, the salt-bridge interaction between Arg^{104}–Glu^{1032} in C4b would be promoted [12]. In addition, given that activated C4b binds to surfaces, it is not known whether these key conformational changes in TED would still occur if C4b were to be bound to a surface. Here, dual polarisation interferometry (DPI) was employed as a sensitive sensor technique that

© 2016 The Author(s). This is an open access article published by Portland Press Limited on behalf of the Biochemical Society and distributed under the Creative Commons Attribution License 4.0 (CC BY).

Biochemical Journal (2016) **473** 4473–4491
DOI: 10.1042/BCJ20160744

measures mass and thickness changes in C4b deposited onto a chip [13]. For example, DPI was shown to detect thickness changes as low as 0.1 nm when calcium ions bind to transglutaminase [14]. AUC monitors size and shape changes of macromolecules in solution [15], and was here used to study monomeric C4b, independently of any effects caused by C4b dimerisation. SAXS resulted in solution structural data for C4b in different NaCl concentrations [16]. The SAXS data enabled the application of a new advanced modelling method to create physically realistic atomistic C4b conformations for comparison with the experimental SAXS curves [17]. These defined the TED–MG1 separation. The three experimental analyses and their atomistic modelling showed for the first time that C4b is seen to form a compact structure in low NaCl concentrations and more extended structures in physiological or high NaCl concentrations, in turn showing that TED is conformationally mobile as a function of the NaCl concentration. This outcome confirmed that both C4b and C3b underwent the same conformational change with the TED domain in low and physiological salt.

Materials and methods

Purification of C4b

C4 was isolated from outdated human plasma obtained from the blood transfusion unit, University College London Hospital, using slight modifications of the published method [18]. Human plasma was dialysed into running buffer containing 85% Buffer A (20 mM HEPES, 50 mM ε-aminocaproic acid, 5 mM EDTA·Na_2, pH 7.4) and 15% Buffer B (as for Buffer A, but including 1 M NaCl) and left overnight at 4°C. The plasma was spun down (Beckman Coulter, Avanti J-30J) to remove precipitates at 11k r.p.m. for 15 min. Supernatant

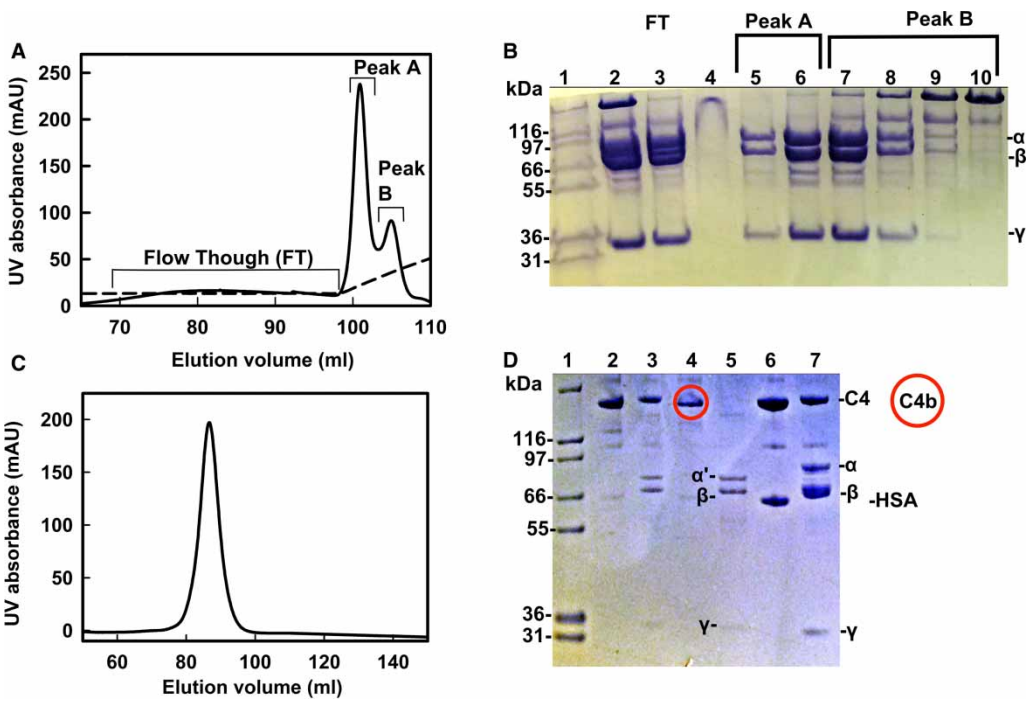

Figure 2. Purification of C4 and C4b.

(**A**) Elution profile of C4 from the HiTrap Heparin HP column. C4 was eluted as peak A, being separately resolved from the α-trypsin inhibitor (peak B). (**B**) Reducing SDS–PAGE analysis of the Heparin HP elution. Lane 1, Mark 12™ molecular mass standard; Lane 2, C4-containing pool before application to the heparin column; Lane 3, flow-through from heparin column; Lanes 5 and 6, peak A showing the α, β and γ chains of C4; Lanes 7–10, peak B showing the bands from α-trypsin inhibitor and C4. (**C**) Gel filtration elution profile of C4b from Superose 6™. (**D**) SDS–PAGE analysis of C4b and C4. Lane 1, Mark 12™ molecular mass standards; Lanes 2 and 3, non-reduced and reduced C4b, respectively, before gel filtration; Lanes 4 and 5, non-reduced and reduced C4b, respectively, after gel filtration, showing the intact protein and its α′, β and γ chains, respectively; Lanes 6 and 7, non-reduced and reduced C4 before the heparin column stage. The α and β chains of C4b are indicated; the α-band shifts to α′ on activation of C4 to C4b. The HSA contaminant is human serum albumin.

© 2016 The Author(s). This is an open access article published by Portland Press Limited on behalf of the Biochemical Society and distributed under the Creative Commons Attribution License 4.0 (CC BY).

Biochemical Journal (2016) 473 4473–4491
DOI: 10.1042/BCJ20160744

(10 ml) was loaded onto a 20 ml Q-Sepharose fast flow anion exchange column (Amersham Biosciences) for separations based on isoelectric points. Non-specifically bound proteins were first eluted with five column volumes of running buffer. Next, C4 was eluted using a 200 ml linear salt gradient from 150 to 500 mM NaCl. Reducing SDS–PAGE (10%) confirmed the presence of the α-chain (97 kDa), β-chain (75 kDa) and γ-chain (33 kDa) (not shown). The C4 fractions eluted between 300 and 350 mM NaCl were dialysed against running buffer for the Mono Q 5/50 GL ion exchange column (GE Healthcare). C4 fractions (20 ml) were loaded for elution using a salt gradient from 150 to 500 mM NaCl. C4 eluted at 380 mM NaCl and the fractions were checked by reducing SDS–PAGE (10%) to confirm the presence of intact C4 from the α, β and γ bands (not shown). The contaminant α-trypsin inhibitor (222 kDa) was removed by passing the C4 fractions through a 5 ml HiTrap Heparin HP column pre-equilibrated with Buffer C (50 mM Tris–HCl, 90 mM NaCl and 0.5 mM EDTA, pH 7.4) (Figure 2A) [19]. The flow-through with some C4 was collected for reuse, and the column was washed with one volume of Buffer C. Bound C4 was eluted using 35 ml of a linear salt gradient from 90 mM to 1 M NaCl. C4 eluted between 170 and 230 mM NaCl (lane 6, Figure 2B), and an α-trypsin inhibitor was eluted between 250 and 400 mM NaCl (lanes 9 and 10, Figure 2B).

C4b was produced by treating 1 mg/ml C4 in HEPES buffer (10 mM HEPES, 137 mM NaCl and 0.5 mM EDTA, pH 7.4) with 20 μg of activated C1s (Complement Tech, U.S.A.) for 60 min at 37°C. The reaction was stopped by adding 0.5 mM diisopropyl fluorophosphate. For AUC and SAXS experiments, the reactive thioester group was blocked with 20 mM iodoacetamide, which was added to the mixture and incubated in the dark at 20°C for 30 min. To make biotinylated C4b for DPI experiments, 1 mg of the maleimide–PEG-2–biotin linker (Thermo Fisher Scientific) was added to the mixture instead of iodoacetamide and incubated for 1 h. An excess biotin linker was removed by dialysis of C4b against HEPES buffer overnight. Finally, the iodoacetamide-treated C4b or biotinylated C4b was concentrated and passed through a Superose™ 6 prep grade XK 16/60 size-exclusion column shortly prior to experiments to remove aggregates (Figure 2C). SDS–PAGE confirmed the presence of C4b (lane 5, Figure 2D) and not C4 (lane 7, Figure 2D).

DPI measurements of C4b

To measure the physical parameters of a layer deposited on the surface of a sensor chip, the *Ana*Light® Bio200 dual-polarization interferometer (Farfield Sensor Ltd, Salford, U.K.) was used [13]. A DPI sensor chip consists of two waveguides stacked one on top of each other. The upper waveguide is exposed to changes from biomolecular interactions and is the sensing waveguide upon which the sample and reference channels (15 mm × 1 mm) are mounted. The lower waveguide is the reference waveguide with a constant refractive index. Two polarisations of laser light (transverse magnetic T_M and transverse electric T_E) are used to detect changes in protein binding. As proteins are added to the sample and reference channels on the sensor waveguide, the effective refractive index of the sensor waveguide is changed for each polarisation (T_E and T_M). These lead to phase changes in the interference patterns generated by the sensing and reference waveguides, and enable the thickness and mass of the added layer to be resolved mathematically [20].

An amine *Ana*Chip® was used for the DPI experiments. The free amine groups on the waveguide surface were modified by a NHS–PEG4–biotin linker [2 mg in 500 μl of phosphate-buffered saline (PBS; 137 mM NaCl, 8.1 mM Na_2HPO_4, 2.7 mM KCl and 1.5 mM KH_2PO_4, pH 7.4); Thermo/Fisher Scientific, Loughborough, U.K.]. An NHS–PEG4–biotin linker (200 μl) was placed on top of the sample and reference channels and left for 2 hours. Excess PBS was washed off with deionised water and the sensor chip left to dry. The prepared chip was then inserted into the DPI machine. The sensor chip structure and the refractive index of the running buffer (10 mM HEPES and 50 mM NaCl, pH 7.4) were calibrated using both 80% (w/w) ethanol/water and water before the experiment, and the linearity of the phase measurement was calibrated from the ethanol to water transition using the *Ana*light® analysis software. Experimental measurements were made at 20°C with a flow rate of 50 μl/min. HEPES buffers with six NaCl concentrations from 75 to 250 mM were injected over the bare surface. The responses were recorded and used to calibrate the refractive indices of the salt solutions. NeutrAvidin (40 μg/ml) was immobilised onto the biotin surface at a flow rate of 60 μl/min, followed by rinsing of the surface with 10 mM HEPES and 2 M NaCl, pH 7.4, buffer at a flow rate of 50 μl/min for 2 min. HEPES buffer with the six different NaCl concentrations was then injected over the NeutrAvidin surface and the responses were recorded. Once the baseline stabilised, 120 μl of biotinylated C4b (30 μg/ml) was injected over the sample channel on top of the NeutrAvidin layer at a flow rate of 20 μl/min. After stabilisation, the NaCl solutions were injected once more to probe the C4b structure. The mass, thickness and

© 2016 The Author(s). This is an open access article published by Portland Press Limited on behalf of the Biochemical Society and distributed under the Creative Commons Attribution License 4.0 (CC BY).

Biochemical Journal (2016) **473** 4473–4491
DOI: 10.1042/BCJ20160744

density changes for the NeutrAvidin and C4b layers during each buffer injection were calculated from the raw data using the *Ana*light® analysis software (Farfield Sensors Ltd, Salford, U.K.).

AUC measurements of C4b

AUC sedimentation velocity data for C4b were collected on two Beckman XL-I analytical ultracentrifuges (Beckman Coulter, Inc., Palo Alto, CA) [15]. A total of 130 absorbance and interference scans were acquired in sedimentation velocity experiments at 20°C with rotor speeds of 50 000 r.p.m. in two-sector cells with a column height of 12 mm. C4b was dialysed into 10 mM HEPES containing 50 or 137 mM NaCl, pH 7.4. The C4b concentrations were 0.25, 0.5, 0.75 and 1.0 mg/ml. The buffer density was measured using an Anton-Paar DMA 5000 density meter to be 1.00487 and 1.00195 g/ml for the 137 and 50 mM NaCl buffers, respectively. SEDFIT version 14.6 was used to fit the experimental boundaries directly according to the Lamm equation [21]. Size-distribution analyses $c(s)$ were produced by SEDFIT that assumed that all species have the same frictional ratio f/f_o. The final SEDFIT analyses used a fixed resolution of 200, and the $c(s)$ fit was optimised by floating the meniscus and the cell bottom until the root mean square deviations and the fit became satisfactory. The f/f_o value used was held at 1.45 to follow that used in the C3b study [10] and this is insensitive to the shape and mass changes being observed. The C4b concentrations were determined using an absorption coefficient of 9.5 (1% concentration, wavelength 280 nm and 1 cm path length) calculated from its composition (UNIPROT code P0C0L4 for the C4A allotype), assuming the presence of four oligomannose and complex-type oligosaccharides at Asn207 (β-chain) and at Asn843, Asn1309 and Asn1372 (α-chain) [22,23]. The sequence-predicted molecular masses of C4 and C4b (including four *N*-glycan chains) were 200.5 and 188.0 kDa, respectively. A partial specific volume of 0.736 ml/g was calculated for C4b from its composition [24].

SAXS measurements of C4b

SAXS data for C4b in three different NaCl concentrations were obtained on the BioSAXS robot at the BM29 beamline at European Synchrotron Radiation Facility, Grenoble, France (ESRF) [25,26]. The data were collected in 16-bunch mode using beam currents from 65 to 78 mA. Data were recorded using a CMOS hybrid pixel Pilatus 1 M detector with a resolution of 981 × 1043 pixels (pixel size of 172 μm × 172 μm). The sample detector distance was 3.0 m. The C4b concentrations were 0.6, 0.8, 1.0 and 1.2 mg/ml. An exposure time of 1 s/frame was used and radiation damage was not observed in the 10 time frames of each SAXS run.

In a given solute–solvent contrast, the radius of gyration R_G corresponds to the mean square distance of scattering elements from their centre of gravity and is a measure of structural elongation. Guinier analyses of the $I(Q)$ curves at low scattering vectors Q (where $Q = 4\pi \sin\theta/\lambda$; 2θ is the scattering angle and λ is the wavelength) give the R_G value and the forward scattering at zero angle $I(0)$ from the expression [27]:

$$\ln I(Q) = \ln I(0) - R_G^2\, Q^2/3$$

This expression is valid in a $Q{\cdot}R_G$ range up to 1.5. The R_G analyses utilised SCT software on Linux workstations [28]. Indirect transformation of the $I(Q)$ curve measured in reciprocal space into real space gives the distance distribution function $P(r)$ and was carried out using the program GNOM [29]:

$$P(r) = \frac{1}{2\pi^2}\int_0^\infty I(Q)\, Qr \sin(Qr)\, dQ$$

$P(r)$ corresponds to the distribution of distances r between volume elements and gives an alternative calculation of the R_G and $I(0)$ values based on the full scattering curve $I(Q)$. It also gives the most frequently occurring distance M and the maximum dimension of the macromolecule L.

Atomistic modelling of the C4b solution structure

Using the recent C4b crystal structure (PDB ID: 4XAM) [3] as a starting structure, molecular Monte Carlo simulations performed using the SASSIE suite [30] were used to generate a library of 21 000 conformationally varied and physically realistic atomistic C4b models for comparison with the SAXS data. Prior to this simulation, the crystal structure was parametrised in the CHARMM36 force field (including the addition of hydrogen atoms) through the PDB reader component of CHARMM-GUI [31–33]. This parametrised model was then

© 2016 The Author(s). This is an open access article published by Portland Press Limited on behalf of the Biochemical Society and distributed under the Creative Commons Attribution License 4.0 (CC BY).

Biochemical Journal (2016) **473** 4473–4491
DOI: 10.1042/BCJ20160744

subjected to energy minimisation to remove steric overlaps. The Monte Carlo simulation proceeded by sampling the ψ and ϕ backbone dihedral angles of defined flexible protein linkers (Figure 1C). One strand ran from the MG1–MG8 core to the TED (Linker 1 and Linker 2), and the other returned from TED back to the MG core (Linker 3 and Linker 4). The linker sequences in that order were E^{933}KEGA^{937}, P^{984}LDLG^{989}, T^{1322}EERG^{1326} and V^{1387}LDMKNTTC^{1394}. Models were generated by varying Linker 1 and Linker 2 using the complex Monte Carlo module of SASSIE. In each Monte Carlo move, all residues after the last residue of Linker 1 [including both the CUB (C1r/C1s–UEGF–BMP1) domain and the TED] or Linker 2 (TED only) were moved. To retain the correct conformation to the rest of C4b, the returning strands were severed at the ends of Linker 3 and Linker 4. To prevent the sampling of non-physical conformations of C4b, distance constraints of 1.4 and 2.3 nm were placed between the first and last residues in each of Linker 3 and Linker 4, respectively. These constraints replicated the linker lengths seen in the C4b crystal structure [3]. Three conformational ensembles were generated: (i) only Linker 1 was varied, creating 10 000 conformers of C4b in which both the CUB domain and the TED moved as one fixed entity; (ii) only Linker 2 was varied, resulting in 2000 conformers with the CUB domain held fixed in the position observed in the C4b crystal structure, but with variable TED positions and (iii) only Linker 2 was varied, but this time using the best-fit CUB domain position from the first ensemble to create 9000 conformers. A steric overlap between the 11 C4b domains (Figure 1C) was excluded by SASSIE. Theoretical scattering curves were generated for the resulting 21 000 C4b conformers using SCT [28], for comparison with the experimental SAXS curves. A cube of side length of 0.540 nm in combination with a cut-off of four atoms was used to convert the C4b atomic co-ordinates into Debye sphere models. The sphere models corresponded to the unhydrated structures. In SAXS experiments, a hydration shell containing 0.3 g of H_2O/g of protein is visible [34]; hydration spheres were added in SCT to replicate this. SCT compared the theoretical scattering from each model to the experimental curves, with the quality of fit quantified using the *R*-factor:

$$R\text{-factor} = \frac{\sum \left| \left| |I_{\text{Expt}}(Q)| - \eta |I_{\text{Theor}}(Q)| \right| \right|}{\sum \left| |I_{\text{Expt}}(Q)| \right|}$$

where $I_{\text{Expt}}(Q)$ represents the experimental data at each Q value, $I_{\text{Theor}}(Q)$ represents the theoretical values and η the scaling factor necessary to compare them. R_G values were calculated from the modelled curves in the same Q ranges used for the experimental Guinier R_G fits. The best-fit models were selected using both the lowest *R*-factor and passing an R_G filter of ±5% of the experimental value. The 100 best-fit atomistic models from each of the 137 and 250 mM NaCl analyses are available in Supplementary Material.

Sedimentation coefficients $s_{20,w}$ for the C4b crystal structure and best-fit scattering models were calculated directly from the atomic coordinates using the HYDROPRO shell-modelling program [35]. The default value of 0.31 nm for the atomic element radius for all atoms was used to represent the hydration shell.

Results

Purification of C4b

For biophysical measurements, C4b was prepared from purified C4. Human C4 and C4u (the thioester-hydrolysed form of C4) from outdated human plasma were separated on an MonoQ column, where C4u was eluted at 300 mM NaCl and C4 at 380 mM NaCl (not shown). In addition, α-trypsin inhibitor co-purified with C4 [18] and was removed using a heparin column (see Materials and Methods). C4 and α-trypsin inhibitor were eluted as separate peaks (Figure 2A,B). Finally, after C1s cleavage of C4, C4b was eluted as a single symmetrical peak from a Superose 6™ gel filtration column (Figure 2C). Reducing (4–12%) SDS–PAGE confirmed the presence of intact C4b α′, β and γ bands, in distinction to the bands seen for C4 where the α-band showed a different mass (lanes 5 and 7, Figure 2D).

DPI analyses of immobilised C4b

DPI measures the interaction between biomolecules in real time without the use of chemical tags by monitoring simultaneously the thickness, mass and density of a biological layer deposited on the surface of a sensor chip [13]. In the DPI instrument, this is achieved by the use of a sensing waveguide and a reference waveguide within the sensor chip, upon which a laser beam with two polarisations T_E and T_M is focused along its length (see Materials and Methods). Following the injection of NeutrAvidin (40 μg/ml) over the biotinylated surface

© 2016 The Author(s). This is an open access article published by Portland Press Limited on behalf of the Biochemical Society and distributed under the Creative Commons Attribution License 4.0 (CC BY).

Biochemical Journal (2016) **473** 4473–4491
DOI: 10.1042/BCJ20160744

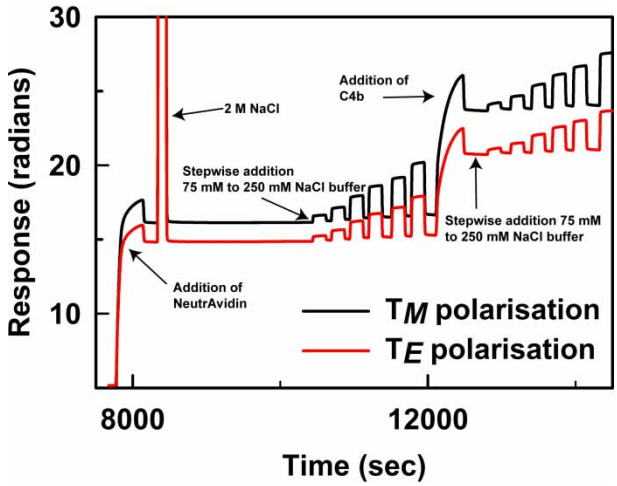

Figure 3. The DPI raw output for the immobilisation of biotinylated C4b on a NeutrAvidin-coated surface.
NeutrAvidin was first flowed over a biotinylated sensor chip at ~8000 s, followed by biotinylated C4b after ~12 000 s. The T_E and T_M polarisations (red and black, respectively) increase between the immobilisations of NeutrAvidin and biotinylated C4b. The T_E and T_M changes with the six buffer injections from 75 to 250 mM NaCl (each separated by the running buffer in 50 mM NaCl) are visible as six peaks.

of the sensing waveguide, the combined changes in the T_E and T_M polarisations (Figure 3) indicated a unique solution that showed a thickness increase of 7.5 nm, a mass increase m_L of 3.1 ng/mm^2 and an average density of 0.416 g/cm^3 (not shown). From these, the surface area A per NeutrAvidin molecule was calculated to be 32 nm^2/molecule (5.7 nm × 5.7 nm/molecule) from the expression $A = M_w/(N_A\ m_L)$ [36], where M_w is the molecular mass of NeutrAvidin (60 kDa) and N_A is Avogadro's number. The area per molecule, in conjunction with the layer thickness, shows whether a single layer or a multilayer structure has been formed. If A is significantly lower than the theoretical saturated value, this indicates a multilayer structure. The maximum theoretical area for NeutrAvidin is 24.6 nm^2/molecule (radius 2.8 nm, measured from the crystal structure of avidin) [37].

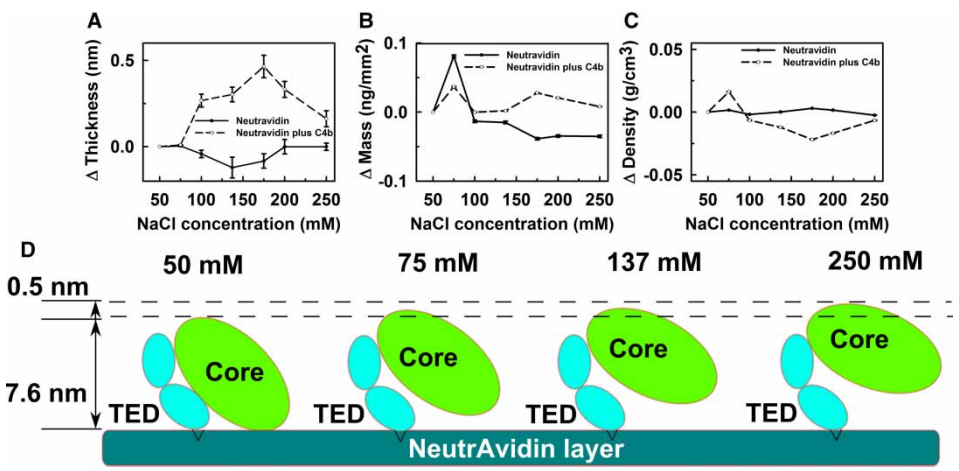

Figure 4. The thickness, mass and density changes for C4b with increase in NaCl by DPI.
(**A**–**C**) The thickness, mass and density changes, respectively, show the difference between the immobilised NeutrAvidin and C4b layers with an increase in the NaCl concentration. Error bars based on a maximum 5 mrad phase error are shown when visible. (**D**) Postulated movement of the MG1–MG8 core in C4b (not drawn to scale) bound to the NeutraAvidin layer in the presence of different NaCl buffers. The loss of the Arg^{104}–Glu^{1032} salt bridge (Figure 1A) causes TED (cyan) and the MG (green) domains to move apart in high NaCl concentration.

© 2016 The Author(s). This is an open access article published by Portland Press Limited on behalf of the Biochemical Society and distributed under the Creative Commons Attribution License 4.0 (CC BY).

Biochemical Journal (2016) 473 4473–4491
DOI: 10.1042/BCJ20160744

The agreement between the experimental and theoretical areas per molecule indicated that NeutrAvidin has formed a monolayer surface. Successive increases in NaCl concentration were made in the DPI experiment, resulting in the T_M and T_E response data for the NeutrAvidin layer (Figure 3). The thickness, mass and density values in 50 mM NaCl buffer were set as baselines (Figure 4). Successive buffer injections (75–250 mM NaCl) showed no significant thickness increase (Figure 4A). This lack of change indicated that the increase in NaCl concentration had no effect on the NeutrAvidin layer (Figure 4B). This absence of structural changes showed that NeutrAvidin was a suitable base layer for the present study.

Complement C4b was immobilised on the NeutrAvidin-coated sensor surface in its physiological orientation by labelling its free exposed thiol group with biotin (Figure 1A) [38]. The T_M and T_E response data for the C4b injection onto the NeutrAvidin layer occurred at 12 500 s (Figure 3). The observed thickness increase of 7.6 nm in 50 mM NaCl indicated that C4b formed a separate layer on top of the NeutrAvidin layer with a mass increase m_L of 1.93 ng/mm^2 and an average protein density of 0.255 g/cm^3. The experimental area A per C4b molecule was 162 nm^2/molecule (12.7 nm × 12.7 nm/molecule). The theoretical saturated area per molecule value was 63.6 nm^2 (radius 4.5 nm) from the x-axis of its crystal structure (Figure 1A) [3]. Taking the molecular mass of C4b to be 188 kDa, the increase in m_L showed that the molar ratio between C4b and NeutrAvidin was 1:5, showing that one C4b molecule was immobilised for every five NeutrAvidin molecules. This ratio agreed well with that of the experimental areas per molecule of 31 and 154 nm^2/molecule for NeutrAvidin and C4b, respectively. The lower density of immobilised C4b also indicated that fewer C4b molecules were bound on top of the NeutrAvidin layer. Moreover, the increase in thickness of 7.6 nm suggested that bound C4b had adopted a tilted orientation on the NeutrAvidin surface (Figure 4A); the maximum possible increase in the thickness was expected to be 15 nm from the maximum length of the C4b crystal structure along its z-axis (Figure 1A).

To determine the dependence of the C4b structure on different NaCl concentration, six buffers with increased NaCl concentrations were injected over the surface (Figure 3). To determine the changes arising from C4b alone, the observed thickness, mass and density values were subtracted from those for the NeutrAvidin surface, since no changes were observed for NeutrAvidin (see above). The thickness and density profile changes for immobilised C4b were significantly different from those for NeutrAvidin alone (Figure 4A,C). However, the mass change profile for C4b was similar to that for NeutrAvidin (Figure 4B). The thickness change for C4b gradually increased as the NaCl concentration increased, with the biggest increase occurring between 75 and 100 mM NaCl (Figure 4A). Above 100 mM NaCl, the thickness change showed an increase of 0.34 nm within error, and this is the mean of the five values observed for C4b, calculated as a distinct layer between 100 and 250 mM NaCl. Because the C4b mass change was unchanged (Figure 4B), the density of the C4b layer decreased compared for that for NeutrAvidin (Figure 4C). The thickness change showed that the increase in NaCl concentration induced conformational changes of C4b, such that C4b became more extended in its conformation in high NaCl concentrations. The changes are schematically shown in Figure 4D. While the precision of the DPI measurements was at best ∼0.01 nm [39], the maximum possible combined error in the phase change in this experiment was estimated from the phase calibration (linearisation) to be 5 mrad [i.e. 0.04% of the phase change and mass signal for NeutrAvidin or 0.5% for the calculated thickness (0.039 nm) and 1.4% (0.107 nm) for the thickness of C4b]. This was used to calculate the error bars shown in Figure 4A–C.

AUC analyses of C4b in solution

The sedimentation coefficient $s_{20,w}$ monitors the rate of sedimentation of C4b in solution through an AUC cell and is dependent on the shape and molecular mass of C4b [15]. The AUC analyses provide shape information on C4b in solution, in distinction to that obtained for C4b immobilised on surfaces. Sedimentation velocity experiments were performed using four C4b concentrations between 0.25 and 1.0 mg/ml (1.3–5.3 μM) in each of 50 and 137 mM NaCl buffers. This concentration range is comparable to the plasma concentration of C4 which is 0.24 mg/ml, while being less than that of 1.15 mg/ml for C3 [40]. The peaks in the size-distribution analyses $c(s)$ monitor the extent of sample monodispersity, and the shape is monitored through the sedimentation coefficient $s_{20,w}$ of the observed peaks [21]. Data analyses resulted in good boundary fits for C4b using both absorbance and interference optics (left panels, Figure 5). A major peak was visible at all C4b concentrations in 50 and 137 mM NaCl buffers, together with a minor peak at higher S values.

(i) In 137 mM NaCl, the major monomeric peak for C4b showed $s_{20,w}$ values of 7.98 ± 0.08 and 7.97 ± 0.07 S, respectively, for the absorbance and interference data, respectively (Figure 5A,C). The molecular masses derived from the $c(s)$ peaks seen by SEDFIT corresponded to 185 kDa, which agreed well with the expected

© 2016 The Author(s). This is an open access article published by Portland Press Limited on behalf of the Biochemical Society and distributed under the Creative Commons Attribution License 4.0 (CC BY).

Biochemical Journal (2016) **473** 4473–4491
DOI: 10.1042/BCJ20160744

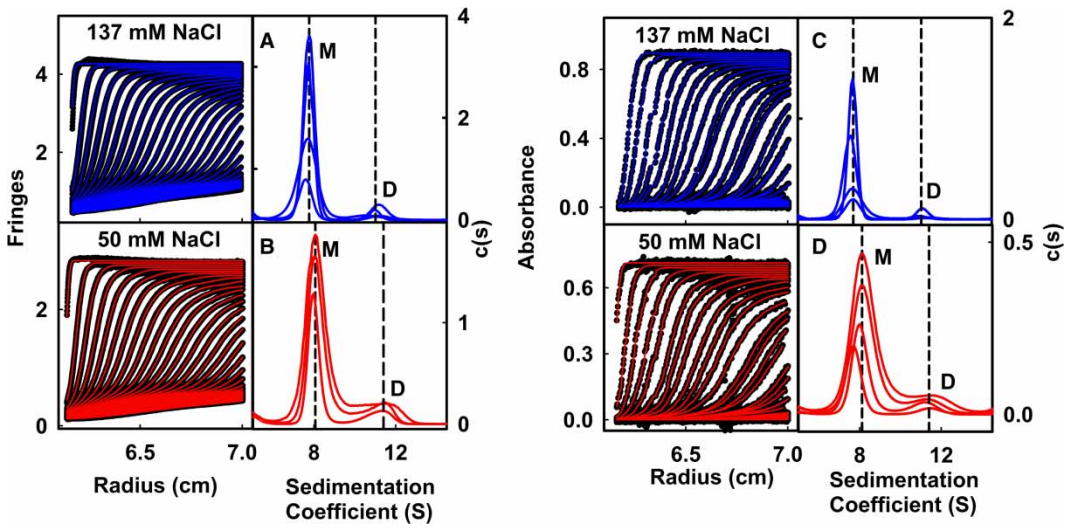

Figure 5. Sedimentation velocity experiments with C4b in 50 and 137 mM NaCl.

(**A** and **B**) The interference boundary fits (left) and the corresponding *c*(s) distributions (right) are shown for C4b in 137 and 50 mM NaCl buffers. For clarity, only every sixth boundary of the 130 that were recorded are shown. (**C** and **D**) The absorbance boundaries fits (left) and the corresponding *c*(s) distributions (right) are shown for C4b in 137 and 50 mM NaCl buffers. For clarity, only every sixth boundary of the 130 boundaries are shown. M, monomer; D, dimer.

monomer molecular mass of C4b of 188 kDa calculated from its sequence-determined composition. The $s_{20,w}$ values showed no concentration dependence, indicating that both the shape and size of C4b were unchanged with different protein concentrations. The minor peak observed at 11.5 S gave a molecular mass of 312 kDa from SEDFIT, which was comparable to the expected value of 376 kDa for a dimer. The lower than expected mass value is most likely to arise from exchange between the monomer and the presumed dimer, but noting that the existence of C4b trimer or tetramer by this approach cannot be definitively ruled out. Peak integration showed that the proportion of the presumed C4b dimer was 9 ± 2%, and the ratio of monomer to dimer resulted in an estimated dissociation constant K_D for the monomer–dimer equilibrium of 25 ± 15 μM.

(ii) In 50 mM NaCl, monomeric C4b gave $s_{20,w}$ values of 8.38 ± 0.14 and 8.41 ± 0.15 S for the absorbance and interference data, respectively (Figure 5B,D). The $s_{20,w}$ values have therefore increased by 0.36–0.45 S, showing that C4b had formed a more compact structure in low NaCl concentration buffer. This $s_{20,w}$ change is similar to the difference seen for the $s_{20,w}$ value for C3b of 7.40 S in 137 mM NaCl, which increased to 7.60 S in 50 mM NaCl [10]. The difference in $s_{20,w}$ values between 50 and 137 mM NaCl is greater than the expected precision of these measurements of ±0.1 S determined from measurements on 79 different AUC instruments [41], although it is noted that all measurements here were made on the same AUC instrument. The molecular masses from the *c*(*s*) peaks corresponded to 185 kDa, which agreed well with the expected value. The presumed dimeric peak observed at 11.5 ± 0.4 S has a molecular mass that corresponded to 323 kDa. The mean $s_{20,w}$ value of the presumed dimer was also increased in 50 mM NaCl compared with that of 11.0 S in 137 mM NaCl, also indicating that the dimer was more compact in shape in low salt. The percentage of dimer was now larger in 50 mM NaCl at 12 ± 1%, and the ratio of monomer to dimer gave an estimated K_D value for the monomer–dimer equilibrium of 20 ± 15 μM. The $s_{20,w}$ value of the C4b dimer peak was similar to that of 11.8 and 12.1 S calculated for the back-to-back dimer seen in one of the C3b crystal structures (PDB ID: 2WIN) [9], suggesting that this was indeed a C4b dimer.

SAXS analyses of C4b in solution

SAXS is a diffraction technique used to study the overall structure of biological molecules in random orientations in solution [16]. Thus, SAXS data enabled the structural conformation of C4b to be studied in solution. The scattering data *I*(*Q*) were collected at C4b concentrations between 0.6 and 1.2 mg/ml for C4b in three

© 2016 The Author(s). This is an open access article published by Portland Press Limited on behalf of the Biochemical Society and distributed under the Creative Commons Attribution License 4.0 (CC BY).

Biochemical Journal (2016) 473 4473–4491
DOI: 10.1042/BCJ20160744

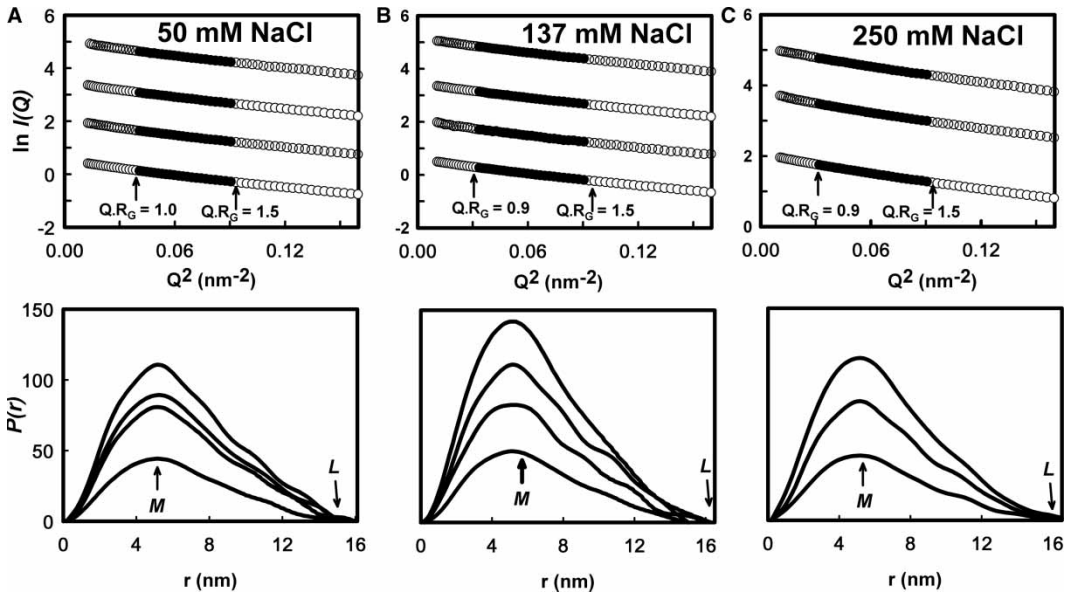

Figure 6. Guinier R_G and distance distribution function $P(r)$ analyses for C4b.

In the X-ray Guinier plots for C4b (upper panels), the fit ranges used to determine the R_G values are denoted by filled circles, together with satisfactory $Q \cdot R_G$ ranges as labelled. Panels **A**, **B** and **C** correspond to buffers containing 50 mM NaCl, 137 mM NaCl and 250 mM NaCl respectively. The Q ranges used for fits were 0.21–0.30 nm^{-1} for 50 mM NaCl and 0.18–0.30 nm^{-1} for 137 mM and 250 mM NaCl. The C4b concentrations were 0.6, 0.8, 1.0 and 1.2 mg/ml for 50 mM and 137 mM NaCl, and 0.6, 0.8 and 1.2 mg/ml for 250 mM NaCl.

NaCl buffers (50, 137 and 250 mM) to match the DPI experiments. No radiation damage effects were observed.

(i) Guinier analyses at low Q ranges in the scattering curves gave R_G values that monitored the overall structure of C4b and its degree of elongation in different NaCl concentrations. The Q ranges used to fit the Guinier plots resulted in linear plots from which the R_G fits were obtained. The mean R_G values for C4b in 137 and 250 mM NaCl were identical at 4.89 ± 0.06 and 4.90 ± 0.02 nm, respectively (Figure 6B,C). Despite the detection of dimer by AUC, the effect of dimer on the R_G fits was minimised by performing these fits in larger Q ranges with a $Q \cdot R_G$ range from 1.0 upwards. Dimer would feature most strongly at the lowest Q values. In 50 mM NaCl, a slight upturn in the $I(Q)$ intensities at the lowest Q values now reflected the presence of 12% dimers that was observed in the AUC analyses (Figure 6A). For this reason, the R_G fits were performed in a larger Q range than for the two other NaCl concentrations. An R_G value of 4.94 ± 0.02 nm was estimated, and this is an average of the R_G values of the C4b monomer and dimer mixture. If the C4b dimer has an R_G value significantly in excess of 4.9 nm, as expected from the AUC analyses above, the R_G value of the C4b monomer will be less than the R_G values of 4.89–4.90 nm for C4b measured in 137 and 250 mM NaCl. This reasoning shows that C4b will be more compact in shape in 50 mM NaCl.

(ii) The distance distribution function $P(r)$ curves were calculated from the full scattering curves and represent all the distances between pairs of atoms within C4b (Figure 6). The $P(r)$ function also provided an alternative determination of the R_G values. These R_G values were 5.03 ± 0.07 and 5.04 ± 0.05 nm for 137 and 250 mM NaCl, respectively, in agreement with the Guinier analyses. The maximum length L of C4b was determined from the value of r when $P(r) = 0$. L was found to be 16.5 nm for 137 mM NaCl and 17 nm for 250 mM NaCl, which are comparable with the dimensions of 15 nm × 8.5 nm seen with the C4b crystal structure (Figure 1A).

Atomistic scattering modelling of C4b in solution

The recent crystal structure of C4b revealed that the TED and MG1 domains were connected by an Arg^{104}–Glu^{1032} salt bridge to form a compact structure (Figure 1A) [3]. Because the DPI, AUC and SAXS data sets

© 2016 The Author(s). This is an open access article published by Portland Press Limited on behalf of the Biochemical Society and distributed under the Creative Commons Attribution License 4.0 (CC BY).

Biochemical Journal (2016) **473** 4473–4491
DOI: 10.1042/BCJ20160744

each indicated the existence of compact and extended structures in 50 and 137–250 mM NaCl buffers, respectively, a new atomistic modelling procedure based on 21 000 physically realistic trial structures was applied to model the structure of C4b from its scattering curve in 137–250 mM NaCl [17]. The modelling of C4b in 50 mM NaCl was precluded by the presence of C4b dimers. Previously, 4650 structurally randomised models derived from the crystal structure of C3b were used to fit the scattering curves of C3b and C3u in 50 and 137 mM NaCl buffers, to reveal compact and extended conformations, respectively, in these buffers [9,10].

Starting from the C4b crystal structure, this new modelling located the TED and CUB domains by variations in the linker peptides between the TED and CUB domains with 7–10 amino acid residues in each (Figure 1C). Linkers 1 and 2 were each conformationally sampled in three different searches to create the 21 000 C4b models. The first search created 10 000 possible conformations by moving the rigid TED–CUB domain pair (Materials and Methods). The second search created 2000 conformations by moving TED alone. The third search took the best-fit C4b model from the first search and created 9000 conformations by moving TED alone. The curve fits of the models against the experimental curves gave 21 000 goodness-of-fit *R*-factors that were compared with the R_G values of these C4b models to result in a single well-defined minimum (green and orange, Figure 7). Visual inspection showed that a single family of conformers gave good fits to the experimental SAXS curves in both 137 and 250 mM NaCl. The 100 lowest *R*-factors corresponded to models with R_G values within error of the experimental R_G values. For 137 mM NaCl, the best-fit 10 models gave *R*-factors of 4.35–4.39%, and the best-fit 100 models showed *R*-factors up to 4.50%. For 250 mM NaCl, the best-fit 10 models gave *R*-factors of 3.92–3.94%, and the best-fit 100 models showed *R*-factors up to 4.00%. In contrast, the C4b crystal structure with the compact TED–MG1 structure (Figure 1A) gave worsened *R*-factors of 5.6 and 4.7% for the two curves, indicating that this structure did not correspond well to the solution structure of C4b.

Comparisons of the experimental and modelled scattering curves showed that excellent curve fits were obtained, especially at low and high *Q* (Figure 8A,B). The best *R*-factors were 4.35 and 3.94% in 137 and 250 mM NaCl buffers, respectively, in which the reduced second value may reflect a further reduction in the C4b dimers in higher salt. The C4b models had been created without the addition of biantennary complex-type *N*-glycan chains. These glycans were added to Asn207, Asn843, Asn1309 and Asn1372 in the best-fit C4b models in extended conformations [22,23]. The effect on the *R*-factors was minimal and did not affect the conclusions of this study. Comparisons of the experimental C4b scattering curve in 137 mM NaCl with the C4b

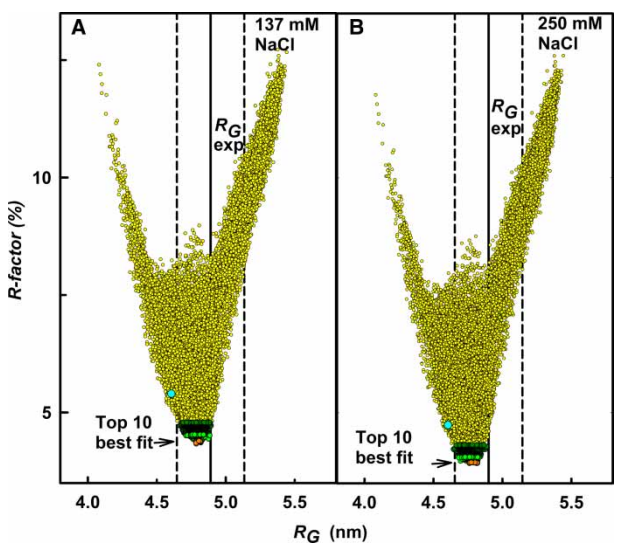

Figure 7. Atomistic scattering modelling analyses of the C4b solution structure.

The X-ray *R*-factors for 21,000 conformational models of C4b in which Linkers 1 and 2 were varied (Figure 1) are compared with their R_G values. Panels **A** and **B** correspond to buffers containing 137 mM NaCl and 250 mM NaCl respectively. The vertical line corresponds to the experimental R_G values, with R_G error ranges of ±5% denoted by dashed lines. The ten, 100 and 700 best fit models from the 21,000 conformations are denoted in orange, green and dark green respectively. The fit for the C4b crystal structure is denoted by the cyan circle at a lower R_G value.

© 2016 The Author(s). This is an open access article published by Portland Press Limited on behalf of the Biochemical Society and distributed under the Creative Commons Attribution License 4.0 (CC BY).

Biochemical Journal (2016) **473** 4473–4491
DOI: 10.1042/BCJ20160744

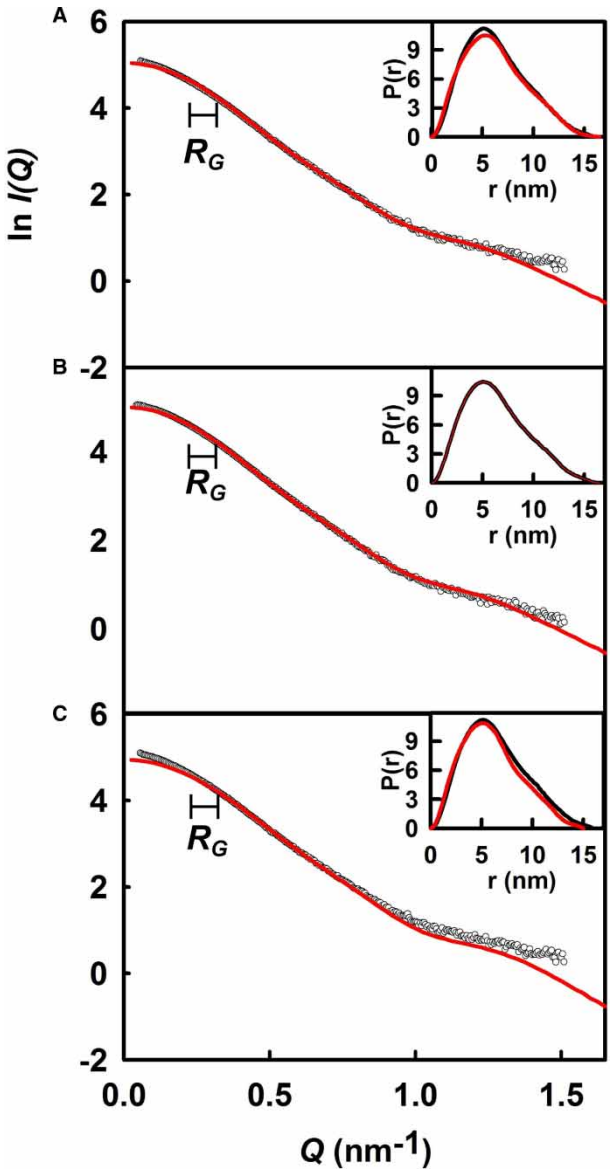

Figure 8. X-ray curve fits for the C4b crystal structure and best-fit solution structures.

The experimental *I*(Q) and *P*(*r*) scattering curves for C4b are shown in black. The theoretical fitted curves are shown in red. (**A** and **B**) The comparison of the best-fit C4b solution structure with the X-ray scattering curves in 137 and 250 mM NaCl are shown, with *R*-factors of 4.3 and 3.9%, respectively (Table 1). (**C**) The comparison of the C4b crystal structure with the X-ray scattering curve of C4b in 137 mM NaCl is shown, giving an *R*-factor of 5.6% (cyan, Figure 7).

crystal structure showed slight but visible differences both at low Q and high Q (Figure 8C). The $P(r)$ curves also showed differences in large r values. The discrepancy at low Q corresponds to different R_G values between the crystal and solution structures, whereas that at high Q corresponds to the different interdomain separations between the TED–CUB pair and the MG1–MG8 core. These differences were readily explained by the separation of the TED and MG1 domains in solution, which were in contact with each other in the crystal structure. As a further test, the $s_{20,w}$ value of the 10 best-fit C4b solution models and the C4b crystal structure were calculated using HYDROPRO. The 10 best-fit C4b models in 137 mM NaCl gave $s_{20,w}$ values of 7.85–7.90 S, which were lower than that of 8.08 S for the C4b crystal structure with the more compact domain arrangement, as expected (Table 1). The 10 best-fit models gave better agreement with the experimental AUC value of 7.97 ± 0.08 S than the crystal structure.

© 2016 The Author(s). This is an open access article published by Portland Press Limited on behalf of the Biochemical Society and distributed under the Creative Commons Attribution License 4.0 (CC BY).

Biochemical Journal (2016) **473** 4473–4491
DOI: 10.1042/BCJ20160744

Table 1 X-ray scattering and sedimentation coefficient modelling fits for C4b

	Filter	Number of models	R_G (nm)[1]	*R*-factor (%)	Length *L* (nm)	$s_{20,w}$ (S)
C4b (50 mM NaCl)	Experimental		4.94 ± 0.02 5.01 ± 0.03[2]		16.0	8.38 ± 0.14
C4b (137 mM NaCl)	None	21 000	4.08–5.44	4.3–12.7	n.a	n.a.
	R-factor	700	4.66–4.89	4.3–4.8	n.a	n.a
		100	4.71–4.88	4.3–4.5	n.a	n.a
	Top 10 fits	10	4.78–4.81	4.3–4.4	16–16.5	7.85–7.90
	Best fit	1	4.78	4.3	16.5	7.90
	Experimental		4.89 ± 0.02 5.03 ± 0.07		16.5	7.97 ± 0.08
C4b (250 mM NaCl)	None	21 000	4.08–5.44	3.9–12.6	n.a	n.a.
	R-factor	700	4.64–4.88	3.9–4.3	n.a	n.a
		100	4.68–4.82	3.9–4.3		
	Top 10 fits	10	4.76–4.81	3.9–3.9	16–17	7.90–8.01
	Best fit	1	4.81	3.9	16.5	7.95
	Experimental		4.90 ± 0.02 5.04 ± 0.05		17.0	n.a

[1]The first experimental R_G value is from the Guinier analyses; the second experimental R_G value is from the *P*(*r*) analyses.
[2]The experimental R_G values in 50 mM NaCl were affected by up to 12% dimer formation and were not used further, although the $s_{20,w}$ value was unaffected by this (Results).
n.a. means not available.

The outcome of the C4b conformational searches was now evaluated. To assess the C4b conformations generated in the 21 000 models, the distances between the centres of mass of TED and the MG1 domain were monitored. This histogram showed that the most common distance was ∼5.5 nm and the frequency of the larger distances decreases above 8 nm up to 15 nm (Figure 9A). To establish that no conformational variation in the best-fit models had been overlooked, the top 100 models were compared with the top 700 models. For the 137 mM NaCl fits, the 700 best-fit models showed that the most common TED–MG1 separation is 4.7 ± 0.1 nm and no model showed a distance over 5.7 nm (Figure 9B). A similar outcome resulted with the 100 best-fit models with a separation of 4.7 ± 0.1 nm. For the 250 mM NaCl fits, the most common distance was again 4.8 ± 0.1 nm and again no model showed a distance over 5.7 nm (Figure 9C). The superimposition of the 10 best-fit C4b models in 137 and 250 mM NaCl showed that these were structurally similar to each other (Figure 10A,B). Three-dimensional density plots showed that the 21 000 C4b models generated in the conformational search had sampled all orientations, shown as a black outline grid in Figure 10C,D. In confirmation of the modelling searches, the 700 best-fit models occupied a limited distribution of positions. This distribution was further contracted when only the 100 best-fit models were considered. All these best-fit models showed that TED and the MG1 domain were close to each other, but not in actual contact with each other, meaning that the Arg^{104}–Glu^{1032} salt bridge has ruptured. In confirmation of this result, these modelled separations of 4.7–4.8 nm were larger than that of 4.0 nm seen in the compact C4b crystal structure (PDB ID: 4XAM) [3]. The corresponding TED–MG1 separations in four C3b crystal structures were within error of this at 3.8 ± 0.4 nm [9,10].

Discussion

The present study showed that the extended and compact structures in C4b play a major role on the overall conformation of C4b, which in turn affects its molecular mechanism for its function and its regulatory control. C4b was shown to be more compact in 50 mM NaCl, when the TED and MG1 domain are in contact with each other through salt-bridge formation. C4b was more extended in physiological 137 mM NaCl buffer, which prevails in serum, when the salt-bridge interaction is broken. Importantly, using a combination of a sensor

© 2016 The Author(s). This is an open access article published by Portland Press Limited on behalf of the Biochemical Society and distributed under the Creative Commons Attribution License 4.0 (CC BY).

Biochemical Journal (2016) **473** 4473–4491
DOI: 10.1042/BCJ20160744

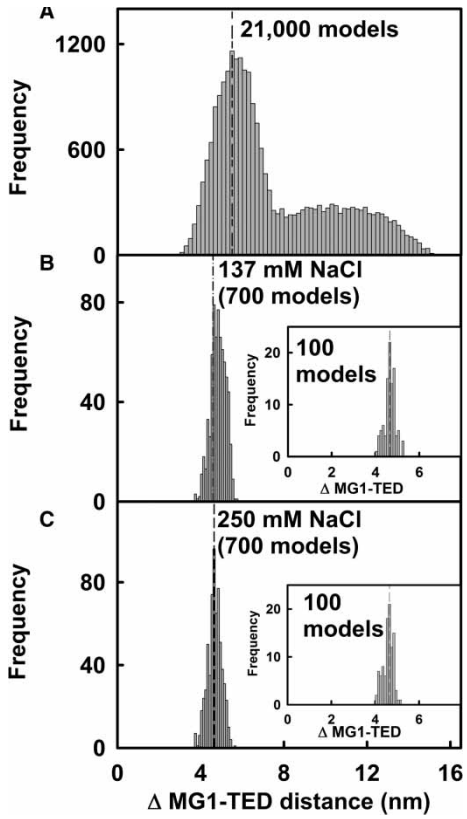

Figure 9. Histograms of the best-fit C4b conformational models.

(**A**–**C**) The three histograms summarise the distribution of the separations between the centres of mass of the TED and MG1 domains in the modelling fits. First, that for all 21 000 conformational models is shown. Next, the histograms for the 700 best-fit models in 137 mM NaCl buffer (dark green in Figure 7A), with the 100 best-fit models shown in the inset (light green in Figure 7A). The broken line indicates the average TED–MG1 separation of 4.7 nm. Finally, the corresponding histograms for the 700 and 100 best-fit models for 250 mM NaCl buffer from Figure 7B are shown.

surface technology (DPI) and two solution technologies (AUC and SAXS), we showed that this conformational change occurred both at surfaces and in solution. The extent of the conformational change was large enough to be detected by DPI and AUC, and by SAXS only in 137–250 mM NaCl, and its magnitude was determined by DPI and by a new atomistic SAXS modelling method (Figure 10A,B). The results for C4b concur with our earlier NaCl concentration solution studies of complement C3b and C3u of the alternative pathway of complement activation, which showed the same result [9,10]. Both C4b and C3b share the same 12-domain structure. However, C4 and C4b are important in relation to only the classical and lectin activation pathways, whereas C3 and C3b are centrally important for complement function as well as functioning in the alternative pathway of activation. A BLAST alignment comparison showed that C4b shared a 30.4% sequence identity with C3b, and their molecular masses were 5% different at 188.0 and 179.3 kDa, respectively. Despite these differences, for the first time, we show that the same ionic strength-mediated conformational change occurs in both C4b and C3b.

This conformational change in C4b and C3b is important for both the regulatory control of complement activation and in disease mechanisms. Crystallographic studies have clarified how five complement regulators bind to active C3b. These C3b complexes include as ligands Factor H short complement regulator domains (SCR) 1/4, membrane cofactor protein (MCP) SCR-3/4, complement receptor type 1 SCR-15/17, decay acceleration factor SCR-2/4 and variola virus SPICE SCR-1/4 [42,43]. All five crystal structures showed that the complexes between C3b and its SCR regulator involve contacts between the MG2 domain in C3b and the first SCR domain of the SCR pair, together with contacts between TED and the second SCR domain of the pair (Figure 10E). Thus, complex formation with the regulator can only occur if the TED–CUB domain pair is in the closed conformation seen in low salt. The Arg^{102}–Glu^{1032} salt bridge in C3b and the Arg^{104}–Glu^{1032} salt bridge in C4b help to stabilise this complex [42,43]. The importance of the

© 2016 The Author(s). This is an open access article published by Portland Press Limited on behalf of the Biochemical Society and distributed under the Creative Commons Attribution License 4.0 (CC BY).

Biochemical Journal (2016) **473** 4473–4491
DOI: 10.1042/BCJ20160744

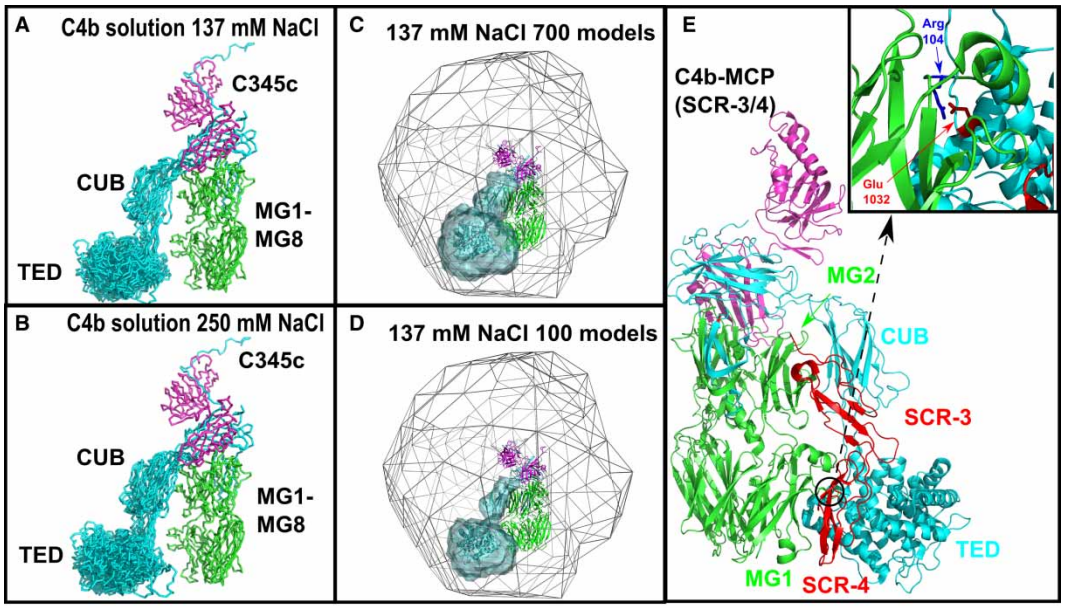

Figure 10. The best-fit C4b conformational models and their functional implication.

(**A** and **B**) The 10 best-fit C4b solution structures that fitted the X-ray scattering curves in 137 and 250 mM NaCl are shown. The α, β and γ chains of C4b are shown in green, cyan and pink, respectively (Figure 1A). The MG core structures were superimposed upon each other to show the variation in position of the 10 TED–CUB domain pairs. (**C** and **D**) The best-fit C4b solution structures are represented as density plots. The grey outline grid shows the boundary of the 21 000 TED and CUB locations in the C4b conformational models. The location of the TED and CUB domains in (**C**) the 700 best-fit and (**D**) 100 best-fit structures for the fits in 137 mM NaCl are shown as cyan envelopes to follow the colour scheme of Figure 1A. Within this envelope, the best-fit C4b solution structure is shown as a ribbon. (**E**) The crystal structure of C4b was superimposed on the crystal structure of the complex between C3b and MCP SCR-3/4. For reason of clarity, the orientation was rotated by 180° about a vertical axis compared with that of Figure 1A. Inset: The Arg^{104}–Glu^{1032} salt bridge between TED (cyan) and the MG1 domain (green) is highlighted to show its importance in the regulatory breakdown of C4b by its cofactors.

Arg^{102}–Glu^{1032} salt bridge was demonstrated by mutagenesis experiments involving Glu^{1032} in TED [10]. Under physiological conditions in plasma, our data showed that the TED–CUB domain pair will be extended away from the MG core of C4b and C3b, and thus unable to form the regulatory complex. Interestingly, this conformational difference between a fully reactive extended C4b or C3b structure with an exposed thioester bridge in the fluid phase and a compact regulated C4b or C3b structure provides a means of altering the reactivity of C4b or C3b to a less active form when either is bound to its regulator. The efficiency of C3b binding to activator surfaces is affected by the location of TED in C3b [44]. Only solution structural studies have been able to reveal this outcome; the extended structure is presumed to be too flexible to crystallise.

In terms of complement-mediated disease, even though C4b and C3b are functional and structurally related, and while C4 deficiency is linked to autoimmune disease and systemic lupus erythematosus [45], we are not aware of any diseases associated with a C4b missense mutation involving the Arg^{104}–Glu^{1032} salt bridge in C4b. We note that another salt bridge also exists between Glu^{1357} and Arg^{974} in C4b between the CUB and MG2 domains. MCP is another of the main regulators of C4b and C3b akin to Factor H and serves to inactivate C4b and C3b bound to host cell surfaces [46]. Sequence alignment showed that the residues that affected C4b binding to MCP, such as V1155, are also present in C3b. It can be assumed that mutations that affect C4b binding to MCP might also perturb C3b binding with MCP, as revealed by the recent crystal structure of C3b with MCP [42]. Thus, other interactions between the TED–CUB domains and the MG1–MG8 domains in C4b may play a role in disease, although these will relate more closely to the complement regulators than with C4b itself. The well-characterised Arg^{102}–Glu^{1032} salt bridge is crucial for C3b and the Factor H SCR-1/4 domains [47]. The C3b polymorphism R102G that affects the Arg^{102}–Glu^{1032} bridge is linked to AMD and aHUS [10]. Several other C3b mutations are genetically

© 2016 The Author(s). This is an open access article published by Portland Press Limited on behalf of the Biochemical Society and distributed under the Creative Commons Attribution License 4.0 (CC BY).

Biochemical Journal (2016) **473** 4473–4491
DOI: 10.1042/BCJ20160744

associated with aHUS [48,49]. One of these mutations (I1157T) is thought to involve the TED–MG1 separation and reduces C3b binding to MCP and in turn reduces its C3b cleavage by the serine protease factor I [48].

The methods reported here provide a new approach to investigating the flexibility of the major complement proteins C4b and C3b, initially based on a multidisciplinary experimental approach, and followed by advanced SAXS modelling based on the generation and testing of thousands of physically realistic structures [17].

(i) Three sets of experimental data showed that the conformational change of C4b between low and high salt had occurred. By DPI, the immobilisation of C4b via its free thiol group in the thioester bond is analogous to its physiological binding to surfaces during complement activation. Our use of DPI revealed increased thickness changes of up to 0.46 nm in the immobilised C4b surface layer on increase in the NaCl concentration (Figure 4). By AUC, it was possible to identify C4b monomer and dimer (Figure 5), as witnessed previously [50], and monomeric C4b sedimented more slowly by 0.4 S in physiological salt compared with low salt (Table 1). Similar slower sedimentation rates were likewise seen for C3b and C3u in physiological buffer. C3, C3b and C3u underwent dimer self-association of 3, 2 and 8%, respectively, in 137 mM NaCl buffer [9,10], which compares well with that of 5% for C4b. However, C4b unexpectedly formed 12% C4b dimer in 50 mM NaCl; the corresponding amount of C3b dimer was 4%. This higher dimer level for C4b clarified that SAXS could not be used to monitor the C4b solution structure in detail in low salt, thus illustrating the value of our multidisciplinary approach. By SAXS, the R_G value of C4b was found to be 4.89 ± 0.02 nm in 137 mM NaCl, which was similar to that for C3b of 4.90 ± 0.02 nm.

(ii) Our new SAXS modelling extends the original small-sphere modelling of C4, C4u and C4b from X-ray and neutron scattering data [51]. In the absence of any known crystal structures at that time, that early study had reported a two-segmented elongated structure in C4b, i.e. the separate TED–CUB domains and the MG1–MG8 core were already detectable at that time. Presently, the atomistic scattering modelling of C4b from the data obtained in 137 and 250 mM NaCl provided solution structural information on extended structures for C4b, in distinction to the compact C4b structure seen using crystals grown in 0.4 M $MgCl_2$ [3]. This compact conformation for C4b is attributable to crystal packing considerations, which favoured this arrangement during crystal growth, and illustrates the need for approaches to verify the actual solution structure. For C4b, good curve fits starting from known crystal structures were similar to those for other complement proteins [16]. For C4b here, the best *R*-factor values were 4.3 and 3.9% for 137 and 250 mM NaCl, respectively (Table 1). For C3b previously, the best *R*-factor values from 4650 trial conformational models were similar at 2.8 and 2.2%, respectively, for 50 and 137 mM NaCl [10]. The main advantages of the present atomistic SASSIE modelling for C4b, compared with previous with C3b, were the rapid generation of a four-fold increase in the number of C4b models for curve fits, using Monte Carlo variations of dihedral angles, and the better handling of steric overlaps where C4b models show these clashes were discarded at their creation. In addition, the use of force-field representations for the 21 000 C4b models mean that the resulting structures were physically reasonable and offer further insights on the conformation of C4b.

In conclusion, an ensemble of 100 best-fit C4b structures (Supplementary Material) from the SASSIE analyses was determined to represent the C4b solution structure (Figure 10D). These structures permitted an assessment of the conformational changes in C4b. The C4b modelling in 137 and 250 mM NaCl resulted in a best-fit TED–MG1 separation of 4.7 ± 0.1 nm (Figures 9 and 10). These separations were larger than that of 4.0 nm seen in the compact C4b crystal structure (PDB ID: 4XAM) [3]. These fitted dimensions for the best-fit C4b solution structure account not only for the outcomes of the AUC and SAXS solution analyses, but also the surface analyses from DPI which reported a thickness change of 0.46 nm. This detail of atomistic modelling is advantageous by determining a numerical separation for 100 and 700 best-fit C4b structures, which is improved compared with a simple rigid body modelling approach that only fitted four possible C4b conformations for scattering curves measured in a single 100 mM NaCl buffer [3]. Previously, 4–10 best-fit C3b structures were determined in our former and less precise curve modelling analysis. From these, the fitted TED–MG1 separations in C3b were 4.3 ± 0.4 nm (50 mM NaCl) and 5.2 ± 0.5 nm (137 mM NaCl). The value of 4.3 nm agreed with the separation of 3.8 ± 0.4 nm seen in four C3b crystal structures, indicating that both structures showed compact TED–MG1 arrangements (PDB ID: 2I07, 2WIN, 2WII and 2ICF) [5,10]. Thus, both C4b and C3b underwent similar conformational changes with changes in NaCl concentration. This joint experimental and computational approach complements previous methods used to study multidomain protein conformations and their flexibility, and is expected to have high potential in the future. Importantly, they are performed in solution under physiological conditions.

© 2016 The Author(s). This is an open access article published by Portland Press Limited on behalf of the Biochemical Society and distributed under the Creative Commons Attribution License 4.0 (CC BY).

Abbreviations

aHUS, atypical haemolytic uraemic syndrome; AMD, age-related macular degeneration; ANA, anaphylatoxin; AUC, analytical ultracentrifugation; CUB, C1r/C1s–UEGF–BMP1; DPI, dual polarisation interferometry; MASP, mannose-binding lectin-associated serine protease; MCP, membrane cofactor protein; MG1–MG8, macroglobulin domains 1–8; PBS, phosphate-buffered saline; SAXS, small angle X-ray scattering; SCR-1/4, short complement regulator 1/4; TED, thioester-containing domain; α_2M, α_2 macroglobulin.

Author Contribution

K.W.F. and J.G. performed experiments and processed the data; K.W.F. and D.W.W. performed the scattering modelling, and K.W.F., M.J.S. and S.J.P. designed the experiments and wrote the paper.

Funding

K.W.F. was supported by a Medical Research Council [MR/K011715/1] grant and a Medical Research Council CASE PhD studentship jointly with Farfield Scientific. D.W.W. was supported by the CCP-SAS project, a joint Engineering and Physical Sciences Research Council [EP/K039121/1] and National Science Foundation [CHE-1265821] grant.

Acknowledgements

We thank Dr Elizabeth Rodriguez and Dr Ruodan Nan for useful discussions, and Dr Adam Round at the ESRF in Grenoble, France, for excellent instrumental support at BM29.

Competing Interests

The Authors declare that there are no competing interests associated with the manuscript.

References

1 Bohlson, S.S., Fraser, D.A. and Tenner, A.J. (2007) Complement proteins C1q and MBL are pattern recognition molecules that signal immediate and long-term protective immune functions. *Mol. Immunol.* **44**, 33–43 doi:10.1016/j.molimm.2006.06.021

2 Kidmose, R.T., Laursen, N.S., Dobo, J., Kjaer, T.R., Sirotkina, S., Yatime, L. et al. (2012) Structural basis for activation of the complement system by component C4 cleavage. *Proc. Natl. Acad. Sci. U.S.A.* **109**, 15425–15430 doi:10.1073/pnas.1208031109

3 Mortensen, S., Kidmose, R.T., Petersen, S.V., Szilagyi, A., Prohaszka, Z. and Andersen, G.R. (2015) Structural basis for the function of complement component C4 within the classical and lectin pathways of complement. *J. Immunol.* **194**, 5488–5496 doi:10.4049/jimmunol.1500087

4 Dodds, A.W. and Alex Law, S.K. (1998) The phylogeny and evolution of the thioester bond-containing proteins C3, C4 and α2-macroglobulin. *Immunol. Rev.* **166**, 15–26 doi:10.1111/j.1600-065X.1998.tb01249.x

5 Janssen, B.J.C., Christodoulidou, A., McCarthy, A., Lambris, J.D. and Gros, P. (2006) Structure of C3b reveals conformational changes that underlie complement activity. *Nature* **444**, 213–216 doi:10.1038/nature05172

6 Janssen, B.J.C., Huizinga, E.G. Raaijmakers, H.C.A., Roos, A., Daha, M.R., Nilsson-Ekdahl, K. et al. (2005) Structures of complement component C3 provide insights into the function and evolution of immunity. *Nature* **437**, 505–511 doi:10.1038/nature04005

7 Fredslund, F., Laursen, N.S., Roversi, P., Jenner, L., Oliveira, C.L.P., Pedersen, J.S. et al. (2008) Structure of and influence of a tick complement inhibitor on human complement component 5. *Nat. Immunol.* **9**, 753–760 doi:10.1038/ni.1625

8 Aleshin, A.E., Schraufstatter, I.U., Stec, B., Bankston, L.A., Liddington, R.C. and DiScipio, R.G. (2012) Structure of complement C6 suggests a mechanism for initiation and unidirectional, sequential assembly of membrane attack complex (MAC). *J. Biol. Chem.* **287**, 10210–10222 doi:10.1074/jbc.M111.327809

9 Li, K., Gor, J. and Perkins, S.J. (2010) Self-association and domain rearrangements between complement C3 and C3u provide insight into the activation mechanism of C3. *Biochem. J.* **431**, 63–72 doi:10.1042/BJ20100759

10 Rodriguez, E., Nan, R., Li, K., Gor, J. and Perkins, S.J. (2015) A revised mechanism for the activation of complement C3 to C3b: a molecular explanation of a disease-associated polymorphism. *J. Biol. Chem.* **290**, 2334–2350 doi:10.1074/jbc.M114.605691

11 Spencer, K.L., Olson, L.M., Anderson, B.M., Schnetz-Boutaud, N., Scott, W.K., Gallins, P. et al. (2008) C3 R102G polymorphism increases risk of age-related macular degeneration. *Hum. Mol. Genet.* **17**, 1821–1824 doi:10.1093/hmg/ddn075

12 Hendsch, Z.S. and Tidor, B. (1994) Do salt bridges stabilize proteins? A continuum electrostatic analysis. *Prot. Sci.* **3**, 211–226 doi:10.1002/pro.5560030206

13 Escorihuela, J., González-Martínez, M.Á., López-Paz, J.L., Puchades, R., Maquieira, Á. and Gimenez-Romero, D. (2015) Dual-polarization interferometry: a novel technique to light up the nanomolecular world. *Chem. Rev.* **115**, 265–294 doi:10.1021/cr5002063

14 Karim, K., Taylor, J.D., Cullen, D.C., Swann, M.J. and Freeman, N.J. (2007) Measurement of conformational changes in the structure of transglutaminase on binding calcium ions using optical evanescent dual polarisation interferometry. *Anal. Chem.* **79**, 3023–3031 doi:10.1021/ac051254b

15 Cole, J.L., Lary, J.W., Moody, T.P. and Laue, T.M. (2008) Analytical ultracentrifugation: sedimentation velocity and sedimentation equilibrium. *Methods Cell Biol.* **84**, 143–179 doi:10.1016/S0091-679X(07)84006-4

16 Perkins, S.J., Okemefuna, A.I., Fernando, A.N., Bonner, A., Gilbert, H.E. and Furtado, P.B. (2008) X-ray and neutron scattering data and their constrained molecular modeling. *Methods Cell Biol.* **84**, 375–423 doi:10.1016/S0091-679X(07)84013-1

© 2016 The Author(s). This is an open access article published by Portland Press Limited on behalf of the Biochemical Society and distributed under the Creative Commons Attribution License 4.0 (CC BY).

Biochemical Journal (2016) **473** 4473–4491
DOI: 10.1042/BCJ20160744

17 Perkins, S.J., Wright, D.W., Zhang, H., Brookes, E.H., Chen, J., Irving, T.C. et al. (2016) Atomistic modelling of scattering data in the collaborative computational project for small angle scattering (CCP-SAS). *J. Appl. Crystallogr.* **49**, doi:10.1107/S160057671601517X
18 Dodds, A.W. (1993) [3] Small-scale preparation of complement components C3 and C4. *Methods Enzymol.* **223**, 46–61 doi:10.1016/0076-6879(93)23037-N
19 Michalski, C. and Mizon, J. (1998) Process for producing an inter-alpha-trypsin inhibitor concentrate for therapeutic use and concentrate thus obtained. Google Patents
20 Reeves, A. (2004) *Theoretical Studies of One-dimensional and Two-dimensional Photonic Structures*. Ph.D. Thesis, University of Durham
21 Schuck, P. (2000) Size-distribution analysis of macromolecules by sedimentation velocity ultracentrifugation and Lamm equation modeling. *Biophys. J.* **78**, 1606–1619 doi:10.1016/S0006-3495(00)76713-0
22 Chan, A.C. and Atkinson, J.P. (1985) Oligosaccharide structure of human C4. *J. Immunol.* **134**, 1790–1798 PMID:2981921
23 Ritchie, G.E., Moffatt, B.E., Sim, R.B., Morgan, B.P., Dwek, R.A. and Rudd, P.M. (2002) Glycosylation and the complement system. *Chem. Rev.* **102**, 305–320 doi:10.1021/cr990294a
24 Perkins, S.J. (1986) Protein volumes and hydration effects. The calculations of partial specific volumes, neutron scattering matchpoints and 280-nm absorption coefficients for proteins and glycoproteins from amino acid sequences. *Eur. J. Biochem.* **157**, 169–180 doi:10.1111/j.1432-1033.1986.tb09653.x
25 Pernot, P., Round, A., Barrett, R., De Maria Antolinos, A., Gobbo, A., Gordon, E. et al. (2013) Upgraded ESRF BM29 beamline for SAXS on macromolecules in solution. *J. Synchrotron. Radiat.* **20**, 660–664 doi:10.1107/S0909049513010431
26 Round, A., Felisaz, F., Fodinger, L., Gobbo, A., Huet, J., Villard, C. et al. (2015) BioSAXS sample changer: a robotic sample changer for rapid and reliable high-throughput X-ray solution scattering experiments. *Acta Crystallogr. D Biol. Crystallogr.* **71**, 67–75 doi:10.1107/S1399004714026959
27 Glatter, O. and Kratky, O. (1982) Small-Angle X-ray Scattering, Academic Press, New York, NY
28 Wright, D.W. and Perkins, S.J. (2015) *SCT*: a suite of programs for comparing atomistic models with small-angle scattering data. *J. Appl. Cryst.* **48**, 953–961 doi:10.1107/S1600576715007062
29 Semenyuk, A.V. and Svergun, D.I. (1991) GNOM — a program package for small-angle scattering data processing. *J. Appl. Cryst.* **24**, 537–540 doi:10.1107/S002188989100081X
30 Curtis, J.E., Raghunandan, S., Nanda, H. and Krueger, S. (2012) SASSIE: a program to study intrinsically disordered biological molecules and macromolecular ensembles using experimental scattering restraints. *Comput. Phys. Commun.* **183**, 382–389 doi:10.1016/j.cpc.2011.09.010
31 Jo, S., Kim, T., Iyer, V.G. and Im, W. (2008) CHARMM-GUI: a web-based graphical user interface for CHARMM. *J. Comput. Chem.* **29**, 1859–1865 doi:10.1002/jcc.20945
32 MacKerell, A.D., Bashford, D., Bellott, M., Dunbrack, R.L., Evanseck, J.D., Field, M.J. et al. (1998) All-atom empirical potential for molecular modeling and dynamics studies of proteins. *J. Phys. Chem. B* **102**, 3586–3616 doi:10.1021/jp973084f
33 Mackerell, A.D., Feig, M. and Brooks, C.L. (2004) Extending the treatment of backbone energetics in protein force fields: limitations of gas-phase quantum mechanics in reproducing protein conformational distributions in molecular dynamics simulations. *J. Comput. Chem.* **25**, 1400–1415 doi:10.1002/jcc.20065
34 Ashton, A.W., Boehm, M.K., Gallimore, J.R., Pepys, M.B. and Perkins, S.J. (1997) Pentameric and decameric structures in solution of serum amyloid P component by X-ray and neutron scattering and molecular modelling analyses. *J. Mol. Biol.* **272**, 408–422 doi:10.1006/jmbi.1997.1271
35 Garcia de la Torre, J., Huertas, M.L. and Carrasco, B. (2000) Calculation of hydrodynamic properties of globular proteins from their atomic-level structure. *Biophys. J.* **78**, 719–730
36 Ricard-Blum, S., Peel, L.L., Ruggiero, F. and Freeman, N.J. (2006) Dual polarization interferometry characterization of carbohydrate-protein interactions. *Anal. Biochem.* **352**, 252–259 doi:10.1016/j.ab.2006.02.011
37 Rosano, C., Arosio, P. and Bolognesi, M. (1999) The X-ray three-dimensional structure of avidin. *Biomol. Eng.* **16**, 5–12 doi:10.1016/S1050-3862(99)00047-9
38 Bernet, J., Mullick, J., Panse, Y., Parab, P.B. and Sahu, A. (2004) Kinetic analysis of the interactions between vaccinia virus complement control protein and human complement proteins C3b and C4b. *J. Virol.* **78**, 9446–9457 doi:10.1128/JVI.78.17.9446-9457.2004
39 Swann, M.J., Peel, L.L., Carrington, S. and Freeman, N.J. (2004) Dual-polarization interferometry: an analytical technique to measure changes in protein structure in real time, to determine the stoichiometry of binding events, and to differentiate between specific and nonspecific interactions. *Anal. Biochem.* **329**, 190–198 doi:10.1016/j.ab.2004.02.019
40 Kasperska-Zajac, A., Grzanka, A., Machura, E., Misiolek, M., Mazur, B. and Jochem, J. (2013) Increased serum complement C3 and C4 concentrations and their relation to severity of chronic spontaneous urticaria and CRP concentration. *J. Inflamm.* **10**, 22 doi:10.1186/1476-9255-10-22
41 Zhao, H., Ghirlando, R., Alfonso, C., Arisaka, F., Attali, I., Bain, D.L. et al. (2015) A multilaboratory comparison of calibration accuracy and the performance of external references in analytical ultracentrifugation. *PLoS ONE* **10**, e0126420 doi:10.1371/journal.pone.0126420
42 Forneris, F., Wu, J., Xue, X., Ricklin, D., Lin, Z., Sfyroera, G. et al. (2016) Regulators of complement activity mediate inhibitory mechanisms through a common C3b-binding mode. *EMBO J.* **35**, 1133–1149 doi:10.15252/embj.201593673
43 Wu, J., Wu, Y.-Q., Ricklin, D., Janssen, B.J.C., Lambris, J.D. and Gros, P. (2009) Structure of complement fragment C3b-factor H and implications for host protection by complement regulators. *Nat. Immunol.* **10**, 728–733 doi:10.1038/ni.1755
44 Alcorlo, M., López-Perrote, A., Delgado, S., Yébenes, H., Subías, M., Rodríguez-Gallego, C. et al. (2015) Structural insights on complement activation. *FEBS J.* **282**, 3883–3891 doi:10.1111/febs.13399
45 Yang, Y., Chung, E.K., Zhou, B., Lhotta, K., Hebert, L.A., Birmingham, D.J. et al. (2004) The intricate role of complement component C4 in human systemic lupus erythematosus. *Curr. Dir. Autoimmun.* **7**, 98–132 doi:10.1159/000075689
46 Barilla-LaBarca, M.L., Liszewski, M.K., Lambris, J.D., Hourcade, D. and Atkinson, J.P. (2002) Role of membrane cofactor protein (CD46) in regulation of C4b and C3b deposited on cells. *J. Immunol.* **168**, 6298–6304 doi:10.4049/jimmunol.168.12.6298
47 Heurich, M., Martinez-Barricarte, R., Francis, N.J., Roberts, D.L., Rodriguez de Cordoba, S., Morgan, B.P. et al. (2011) Common polymorphisms in C3, factor B, and factor H collaborate to determine systemic complement activity and disease risk. *Proc. Natl. Acad. Sci. U.S.A.* **108**, 8761–8766 doi:10.1073/pnas.1019338108

© 2016 The Author(s). This is an open access article published by Portland Press Limited on behalf of the Biochemical Society and distributed under the Creative Commons Attribution License 4.0 (CC BY).

48 Martínez-Barricarte, R., Heurich, M., López-Perrote, A., Tortajada, A., Pinto, S., López-Trascasa, M. et al. (2015) The molecular and structural bases for the association of complement C3 mutations with atypical hemolytic uremic syndrome. *Mol. Immunol.* **66**, 263–273 doi:10.1016/j.molimm.2015.03.248
49 Rodriguez, E., Rallapalli, P.M., Osborne, A.J. and Perkins, S.J. (2014) New functional and structural insights from updated mutational databases for complement factor H, Factor I, membrane cofactor protein and C3. *Biosci. Rep.* **34**, 635–649 doi:10.1042/BSR20140117
50 Masaki, T., Matsumoto, M., Yasuda, R., Levine, R.P., Kitamura, H. and Seya, T. (1991) A covalent dimer of complement C4b serves as a subunit of a novel C5 convertase that involves no C3 derivatives. *J. Immunol.* **147**, 927–932 PMID:1861081
51 Perkins, S.J., Nealis, A.S. and Sim, R.B. (1990) Molecular modeling of human complement component C4 and its fragments by X-ray and neutron solution scattering. *Biochemistry* **29**, 1167–1175 doi:10.1021/bi00457a011

© 2016 The Author(s). This is an open access article published by Portland Press Limited on behalf of the Biochemical Society and distributed under the Creative Commons Attribution License 4.0 (CC BY).